Aneutronic H + ^{11}B nuclear fusion driven by Coulomb explosion of hydrogen nanodroplets

Isidore Last, Shlomo Ron, and Joshua Jortner

School of Chemistry, Tel-Aviv University, Ramat Aviv, Tel Aviv 69978, Israel
(Received 21 November 2010; published 11 April 2011)

We consider a reaction design for table-top nuclear fusion between two distinct nuclei, with high-energy nuclei being produced by a Coulomb explosion (CE) of homonuclear nanodroplets of one reagent reacting with a solid target of a second reagent. This scheme was applied for a theoretical-computational study of the table-top aneutronic $p + {}^{11}\text{B} \rightarrow 3\alpha + 8.7$ MeV reaction generated by a source of high-energy (0.3–6 MeV) protons produced by a CE of hydrogen nanodroplets driven by ultra-intense, femtosecond, near-infrared laser pulses and which penetrate into a solid ^{11}B target. The averaged reaction probability and the yield for $^{11}\text{B}(p,\alpha)2\alpha$ fusion were calculated from the energy-dependent reaction probability, which was obtained from the ratio of the large fusion cross sections and the stopping power of the protons, and by the proton kinetic energy distribution function, which was obtained from scaled electron and ion dynamics simulations. The fusion yields were determined in the nanodroplet size range and in the laser intensity domain, satisfying the conditions of weak laser intensity attenuation within a single nanodroplet and within an assembly of exploding nanodroplets in the macroscopic plasma filament. The highest values of the fusion yield of 10^8 per laser pulse were attained for the largest nanodroplets with initial radii of 200 nm at the laser peak intensity of 10^{19} W cm^{-2}. The $^{11}\text{B}(p,\alpha)2\alpha$ fusion yields for the exploding hydrogen nanodroplet source-solid ^{11}B cylindrical target are higher by three to four orders of magnitude than the yields of $10^4 - 10^5$ per laser pulse from a laser-irradiated mixed boron-hydrocarbon solid and from a CE of boron-hydrogen heteronuclear nanodroplets. The high efficiency for fusion within the exploding nanodroplets source-cylindrical solid target design provides guidelines for the optimization of yields for table-top nuclear fusion.

I. INTRODUCTION

Aneutronic fusion reactions which, in contrast to the $D + D$ and $D + T$ reactions, do not release neutrons, constitute an attractive potential fusion energy source [1–4]. The H + $^{11}\text{B} \rightarrow 3\,^4\text{He} + 8.7$ MeV, $^{11}\text{B}(p,\alpha)2\alpha$ reaction may provide a promising aneutronic fusion fuel cycle [2,3,5]. The utilization of the $^{11}\text{B}(p,\alpha)2\alpha$ reaction in possible future fusion reactors was attempted by magnetic heating [6], colliding beams [7,8], beam ignition [9], spherical inertial confinement of pellets [10], and block ignition by plane geometry irradiation [11]. However, the prospects of gaining a positive energy balance for the $^{11}\text{B}(p,\alpha)2\alpha$ fusion reaction in large-scale facilities remain remote [5,11–13].

The quest for table-top nuclear fusion was recently realized by the energetics and dynamics of large, finite systems at extremes, where ultra-intense laser-matter interaction manifests unique features of Coulomb instability of highly charged matter [14–25]. The exploration of the aneutronic $^{11}\text{B}(p,\alpha)2\alpha$ nuclear fusion driven by Coulomb explosion (CE), which is the subject matter of this paper, will elucidate the characteristics of the reaction design for the optimization of the yields for table-top fusion. Table-top fusion reactions [14–25] can be driven by the irradiation of clusters [14–18,21–23], nanodroplets [19,24,25], or solids [20] containing reagent atoms with ultra-intense, short, near-infrared lasers (peak intensities $I_M = 10^{17}$–10^{21} W cm^{-2}, pulse widths $\tau \sim 10^{-14}$–10^{-12} s). CE of these extremely ionized systems produces high-energy (keV–MeV) nuclei, which generate fusion reactions [14–25]. Experiments were conducted on dd fusion [involving the $D(d,n)^3$He and $D(d,p)T$ reactions] driven by a CE of deuterium containing clusters and nanodroplets [14,19,21,22]. Theoretical-computational studies addressed

the implementation of other fusion and nucleosynthesis reactions involving heavier nuclei [23–26]. Some fusion reactions involving nuclei heavier than tritium, which include the $^{11}\text{B}(p,\alpha)2\alpha$ reaction, can be driven by laser irradiation of solids [27–30]. Generating the $^{11}\text{B}(p,\alpha)2\alpha$ reaction by laser irradiation of a solid mixture of a $(\text{CH}_2)_n$ polymer and ^{11}B to produce energetic protons and ^{11}B nuclei was suggested by Krainov [31] and was realized experimentally by Belyaev *et al.* [28,30]. In that experiment, a maximal yield of $Y = 10^4$ α particles per laser pulse (with a pulse length of 1.5 ps and a pulse energy of 10 J) was observed [30], while theoretical estimates for the optimized yields resulted in $Y \simeq 10^5$ per laser pulse [30].

Efficient table-top fusion driven by a CE of nanodroplets [19,24–26], with a special reference to the $^{11}\text{B}(p,\alpha)2\alpha$ reaction, will be realized under the following conditions: (i) The production of nuclear matter induced by complete inner and complete or partial outer ionization of the nanodroplet [15,17,23]. (ii) Large fusion cross sections, e.g., a resonance with a very high cross-section peak of $\sigma = 1.2 \times 10^{-24}$ cm^2 at energy $E = 630$ keV and an energetic width of $\Delta E(^{11}\text{B} + \text{H}) \simeq 200$ keV for the $^{11}\text{B}(p,\alpha)2\alpha$ reaction, cause this aneutronic fusion to be efficient [3]. (iii) The attainment of ultrahigh center-of-mass energies (300 keV–6 MeV) of the protons, for which the $^{11}\text{B}(p,\alpha)2\alpha$ fusion cross sections reach high values. (iv) The selection of appropriate sources (where high-energy nuclei are produced) and targets (where the reaction occurs) for efficient fusion. The source for fusion generated by a CE of inner or outer ionized clusters and nanostructures constitutes an assembly of nanostructures driven by an ultra-intense laser, while the target involves the macroscopic plasma filament [21–26]. The $^{11}\text{B}(p,\alpha)2\alpha$ fusion reaction can be induced

by a CE of $(B_2H_6)_n$ nanodroplets (in the size domain of $R_0 = 20-100$ nm) driven by an ultra-intense laser (e.g., $I_M = 10^{19}$ W cm^{-2}, and a pulse length of $\tau = 10-100$ fs), in analogy with the $^{12}C(p,\gamma)N^{13}$ reaction driven by a CE of $(CH_4)_n$ nanodroplets [25]. This interesting experiment has not yet been performed. A rough order-of-magnitude estimate for the yields Y per laser pulse of the $^{11}B(p,\alpha)2\alpha$ reaction, which occurs inside the macroscopic laser filament generated by a CE of $(B_2H_6)_n$ nanodroplets, can be obtained by scaling of the yield for the $^{12}C(p,\gamma)^{13}N$ reaction driven by a CE of $(CH_4)_n$ nanodroplets ($\simeq 1$ per laser pulse, at $I_M = 10^{19}$ W cm^{-2} and $\tau = 25$ fs) [25] by the ratio of the energy-weighted cross sections [3,25] for the two fusion reactions, which results in $Y = 10^4 - 10^5$ per pulse. This yield for the $^{11}B(p,\alpha)2\alpha$ reaction driven by a CE of heteronuclear $(B_2H_6)_n$ nanodroplets is similar to the experimental and theoretical yields for this reaction in laser-irradiated mixed $^{11}B + (CH_2)_n$ solids [30].

In this paper we advance and analyze a reaction design for table-top fusion between two distinct nuclei, with high-energy nuclei being produced by a CE of homonuclear nanodroplets of one reagent reacting with a solid target of the second reagent. A similar reaction design (for neutron production) was proposed by Davis *et al.* for the *dd* fusion [32]. We present a theoretical-computational study of the aneutronic $^{11}B(p,\alpha)2\alpha$ fusion reaction generated by a source of high-energy (MeV) protons produced by a CE of hydrogen nanodroplets (initial radii $R_0 = 70-200$ nm) driven by ultra-intense, femtosecond, near-infrared laser pulses ($I_M = 10^{18}-10^{20}$ W cm^{-2}). These high-energy protons then impinge on and penetrate into a solid ^{11}B target. The target constitutes a hollow solid ^{11}B cylinder (Fig. 1). We demonstrate the attainment of a marked enhancement of the table-top fusion yield (10^8 per laser pulse)
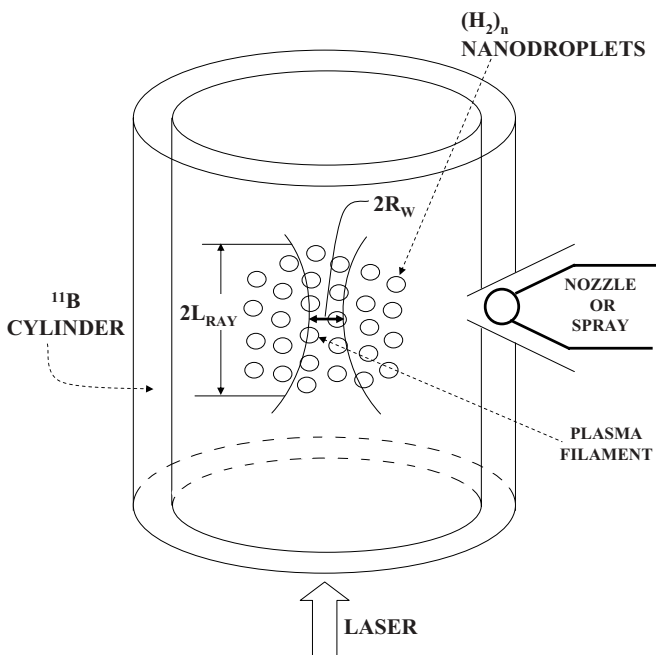

FIG. 1. A schematic description of the cylindrical solid reactor of ^{11}B and of the plasma filament where high-energy protons are produced by a CE of hydrogen nanodroplets.

for the $^{11}B(p,\alpha)2\alpha$ reaction within the reaction design used herein, relative to the considerably lower yields (10^4–10^5 per laser pulse) experimentally accomplished and theoretically estimated for this reaction in laser-irradiated mixed solids [30] and roughly estimated (see above) for CE of heteronuclear boron-hydrogen nanodroplets. The cumulative contributions of the effects of the high proton energies from the exploding homonuclear hydrogen nanodroplets source, in conjunction with the properties of the cylindrical target, result in efficient high-yield, table-top aneutronic fusion.

II. FUSION YIELDS IN A CYLINDRICAL SOLID TARGET

A. Proton energetics

When spherical large finite systems, i.e., clusters ($R_0 \simeq 1-10$ nm) and nanodroplets ($R_0 \simeq 10-1000$ nm), are irradiated by ultra-intense, femtosecond, near-infrared laser pulses, they undergo sequential inner and outer ionization processes followed by a CE of highly charged atomic ions or/and nuclei [15–18,23,33]. In the case of high intensity ($I_M \geqslant 10^{19}$ W cm^{-2}), ultrashort laser pulses (pulse widths of 10–100 fs), the conditions for ultrafast complete and vertical ionization of the large finite system may be realized providing average ion energies that do not depend on the laser radiation intensity, and are described by the scaling law [16–18,34]

$$E_{av} = \frac{4\pi}{5}B\rho q R_0^2, \qquad (1)$$

where q is the ion charge in e units, ρ is the atomic density in nm^{-3}, $B = 1.44 \times 10^{-3}$ keV nm, and E_{av} is obtained in keV. The corresponding maximal CE energy is $E_{max} = (5/3)E_{av}$ [16–18,34]. For hydrogen and deuterium clusters or nanodroplets, $q = 1$ and $\rho = 50$ nm^{-3}. At high values of R_0 and lower values of I_M, the situation of vertical ionization is inapplicable, the energy of the ions becomes dependent on I_M, and the quadratic increase of E_{av} with increasing R_0 is slowed down [16,18,34]. The proton energy required for an effective $^{11}B(p,\alpha)2\alpha$ reaction is in the range of $\geqslant 500$ keV [1,3]. According to Eq. (1), protons with an average energy of 1 MeV are provided by a CE of $(H_2)_n$ nanodroplets with $R_0 = 74$ nm. We conclude that an effective $^{11}B(p,\alpha)2\alpha$ reaction can be generated by a CE of hydrogen nanodroplets with initial radii in the range of $R_0 \gtrsim 70$ nm.

B. Fusion reaction probabilities and yields

We assume that all protons generated by a CE of hydrogen nanodroplets reach the solid ^{11}B surface without energy loss. Such conditions are met when the plasma filament created in the laser focus volume is surrounded by a solid cylinder with a sufficiently small radius to provide free motion of protons in the space between the plasma filament and the cylinder (Fig. 1). The fusion reaction yield per laser pulse is

$$Y = N_p\langle y \rangle, \qquad (2)$$

where N_p is the number of protons produced in the plasma filament and $\langle y \rangle$ is the averaged reaction probability given by

$$\langle y \rangle = \int_0^{E_{max}} P(E)y(E)dE. \qquad (3)$$

Here $P(E)$ is the energy distribution function of the protons with the maximal proton energy E_{max}, and $y(E)$ is the reaction probability for a proton with the initial energy E penetrating into the solid ^{11}B,

$$y(E) = \rho_B \int_0^{\ell(E)} \sigma(E'(x)) dx, \tag{4}$$

where ρ_B is the solid boron atomic density, $\ell(E)$ is the proton penetration depth, E' is the proton energy at depth x, and σ is the reaction cross section. The proton energy losses equation [35] is

$$\frac{dE}{dx} = -\rho_B S(E), \tag{5}$$

with $S(E)$ being the stopping power at energy E [35] normalized to the atomic density of the target. The integral in Eq. (4) can be transformed to the integral over the proton energy E', with the reaction probability being

$$y(E) = \int_0^E \frac{\sigma(E')}{S(E')} dE'. \tag{6}$$

A similar expression for the reaction probability, which is based on the Bethe-Bloch formula for $S(E)$, was presented by Krainov *et al.* [18]. Our approach, which is based on experimental data for $S(E)$ [35], is more accurate.

C. Stopping power of protons in solid ^{11}B

The stopping power $S(E)$ for protons penetrating into a pure ^{11}B boron solid was taken from Ref. [35]. The energy dependence of $S(E)$ at low energies manifests a maximum at $E \approx 70$ keV with a monotonous decrease at $E > 70$ keV. The energy dependence of $S(E)$ in the high-energy interval 200 keV–5 MeV is shown in Fig. 2. It is important to note that $S(E)$ does not depend on the boron body density. Accordingly, the reaction probability y, Eq. (6), is independent of the ^{11}B target density. The penetration depth $\ell(E)$ is inversely proportional to the boron atomic density ρ_B, being determined by the integral

$$\ell(E) = \frac{1}{\rho_B} \int_0^E \frac{dE'}{S(E')}. \tag{7}$$

As expected, the penetration depth, Eq. (7), decreases with increasing the boron density. The dependence of the penetration depth $\ell(E)$ on E for solid boron with $\rho_B = 1.31 \times 10^{23}$ cm^{-3} is shown in Fig. 2. The penetration depth at ~ 1 MeV is ~ 10 μm, increasing to ~ 100 μm at $E = 3.5$ MeV. Accordingly, the wall thickness of the cylinder has to exceed 0.1 cm.

Our theoretical treatment of the fusion probabilities is based on the consideration of reactivity during the stopping of energetic protons within the solid target. This approach is more general and useful than that previously used by Davis *et al.* [32] for the calculations of the $D(d,n)^3$He fusion yields based on a CE of deuterium nanodroplets inside a deuterium-coated cylinder. The present work provides a self-consistent treatment of the energy-dependent, proton penetration depth [Eq. (7)], while Davis *et al.* [32] considered an energy-independent, fixed reaction distance for the nuclei in the solid.

III. REACTION PROBABILITIES AND YIELDS FOR THE ^{11}B(p,α)2α FUSION REACTION

A. Proton-energy-dependent cross sections and reaction probabilities

The energy-dependent cross section for the ^{11}B(p,α)2α reaction was taken from Ref. [3], where it is presented as a function of the center-of-mass energy E_{cm}. This reaction cross section is shown in Fig. 3 as a function of the proton energy $E = 1.091 E_{cm}$ (neglecting the low and very narrow resonance peak at $E \sim 150$ keV). The cross section $\sigma(E)$ manifests a high resonance peak of 1.2×10^{-24} cm^2 at $E = 630$ keV. The energy dependence of $\sigma(E)$ is divided into three domains: (I) $E < E_I$ with $E_I = 330$ keV, where $\sigma(E) = 0$; (II) $E_I < E < E_{II} = 1090$ keV with $\sigma(E)$ exhibiting a resonance peak; and (III) $E_{II} < E < E_{III}$, where σ is changing in a relatively narrow range, i.e., $\sigma = 1.3 \times 10^{-25}$–$2.6 \times 10^{-25}$ cm^2 up to
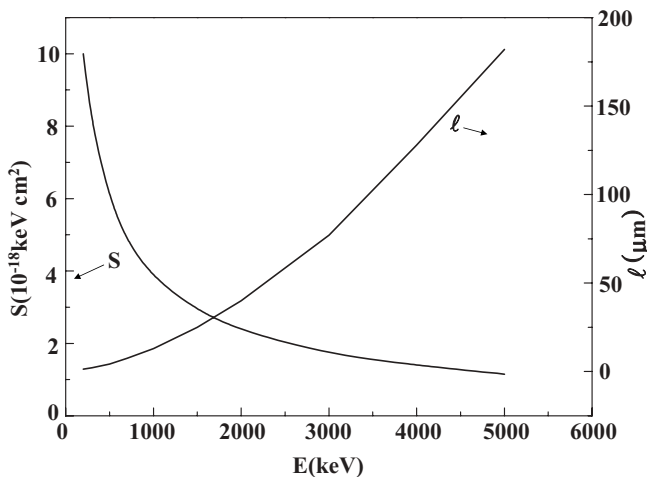

FIG. 2. The energy dependence of the stopping power for protons penetrating into ^{11}B solid (Ref. [35]) and of the penetration depth, Eq. (7).
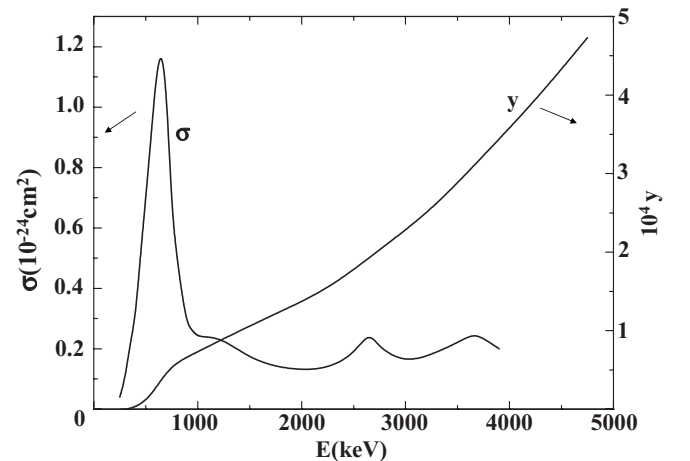

FIG. 3. The energy dependence of the cross section for the $H + ^{11}$B reaction (Ref. [3] and Sec. III A) and of the fusion reaction probabilities, Eqs. (8)–(11).

3800 keV [3] and in a similar range in the energy interval 3800–6000 keV [5]. We take the upper limit for this domain as $E_{III} = 6000$ keV, where $\sigma(E)$ is taken to be constant, being equal to an average value of $\sigma_{III} = 1.8 \times 10^{-25}$ cm^2.

The reaction probability $y(E)$, Eq. (6), was evaluated using the three domains for $\sigma(E)$. In domain I, $\sigma(E) = 0$ and consequently $\langle y \rangle = 0$. In domain II, the reaction probability is presented by the integral

$$y(E) = \int_{E_I}^{E} \frac{\sigma(E')}{S(E')} dE', \quad E_I < E < E_{II}. \tag{8}$$

The results of the numerical integration of Eq. (8) in domain II were fitted by the analytical expression

$$y(E) = \frac{aE^5}{1 + bE^5}, \quad E_I < E < E_{II}, \tag{9}$$

with $a = 3.92 \times 10^{-19}$ keV^{-5} and $b = 4.7 \times 10^{-15}$ keV^{-5}. The total contribution in resonance domain II is $y(E_{II}) = 7.3 \times 10^{-5}$. The reaction probability in domain III is

$$y(E) = y(E_{II}) + \sigma_{III} \int_{E_{II}}^{E} \frac{dE'}{S(E')}, \quad E_{II} < E < E_{III}, \tag{10}$$

where $y(E_{II})$ is given by Eq. (8) for $E = E_{II}$. Using Eq. (7) gives

$$y(E) = y(E_{II}) + \rho B \sigma_{III} [\ell(E) - \ell(E_{II})], \quad E_{II} < E < E_{III}. \tag{10'}$$

The results of the numerical integration of Eq. (10) in domain III were fitted by a quadratic equation,

$$y(E) = y(E_{II}) + c(E - E_{II}) + d(E - E_{II})^2, \quad E_{II} < E < E_{III} \tag{11}$$

with $c = 3.80 \times 10^{-8}$ keV^{-1} and $d = 1.46 \times 10^{-11}$ keV^{-2}.

The dependence of the reaction probability $y(E)$ on the proton energy E, Eqs. (9) and (11), in the energy interval $0 < E < 5000$ keV, is shown in Fig. 3. It is interesting to note that the contribution of the resonance domain II to the reaction yield is dominating only for $E < 2000$ keV. In contrast to fusion reactions with an exponential $\sigma(E)$ dependence [36], the reaction probability $y(E)$ for the ^{11}B$(p,\alpha)2\alpha$ reaction increases moderately with increasing the energy E, at least for $E > 500$ keV, which improves the accuracy of the calculations of the reaction yields.

B. Energetics of a CE of hydrogen nanodroplets

The reaction yields Y, Eqs. (2) and (3), are determined by the kinetic energy distribution $P(E)$. The energies of protons produced by a CE of hydrogen nanodroplets were calculated by scaled electron and ion dynamics (SEID) simulations [37]. The nanodroplet size dependence of the average E_{av} and the maximal E_{max} proton energies in the intensity range $I_M = 10^{18}-10^{20}$ W cm^{-2} ($\tau = 30$ fs), as obtained by these simulations, is presented in Fig. 4. The SEID simulations for a CE of hydrogen nanodroplets with $R_0 \geqslant 100$ nm in the highest laser intensity range of $I_M = 10^{19}-10^{20}$ W cm^{-2} give E_{max} and E_{av} values that exceed 1 MeV. At the highest
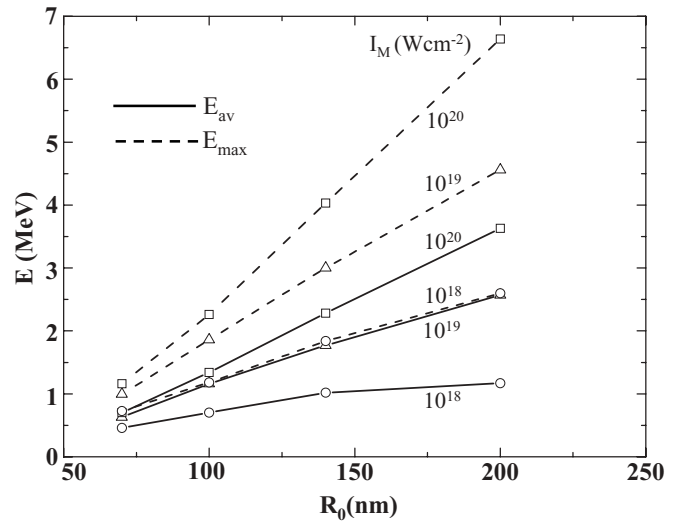

FIG. 4. The size dependence of the energetics of a CE of hydrogen nanodroplets, presenting the dependence of E_{av} and E_{max} on R_0 at laser intensities of $I_M = 10^{18}, 10^{19}$, and 10^{20} W cm^{-2}, and a pulse width of $\tau = 30$ fs.

intensities of $I_M = 10^{20}$ and 10^{19} W cm^{-2}, the energies E_{max} and E_{av} (Fig. 4) manifest the following features: (i) Convergence with decreasing the nanodroplet size, so that at $R_0 = 70$ nm these energies are independent of I_M. (ii) Scaling approximately linearly with R_0^2 in the lower nanodroplet size domain of $R_0 = 70-100$ nm, in agreement with Eq. (1). (iii) The ratio E_{max}/E_{av} for $R_0 = 70-100$ nm is close to 1.7. These characteristics (see Sec. II A) indicate the occurrence of complete and vertical outer ionization of the smaller ($R_0 = 70-100$ nm) nanodroplets at the highest intensities of $I_M = 10^{19}-10^{20}$ W cm^{-2}. For larger nanodroplets with $R_0 \geqslant 100$ nm at the highest intensities of $I_M = 10^{19}-10^{20}$ W cm^{-2} and over the entire size domain at the lower intensity of $I_M = 10^{18}$ W cm^{-2}, the energies E_{max} and E_{av} show a marked intensity dependence at fixed R_0 and reveal marked deviations from the scaling law $E_{max}, E_{av} \mu R_0^2$ (Fig. 4), indicating incomplete and nonvertical outer ionization of the nanodroplet. Most importantly, at the two highest intensities, the kinetic energy distribution $P(E)$ is well described (Fig. 5) by the relation [16,18,34]

$$P(E) = (3/2E_{max}) (E/E_{max})^{1/2}, \tag{12}$$

which for $R_0 = 70$ nm and $I_M = 10^{20}$ W cm^{-2} corresponds to complete and vertical outer ionization. The data for the energetics of a CE of nanodroplets presented in this section should, however, constitute upper limits as they do not take into account the effect of the attenuation of the laser light propagating inside a nanodroplet [25,38].

C. Laser intensity attenuation within a nanodroplet

The intensity attenuation of the laser light inside a single nanodroplet is expected to markedly decrease the energy of ions produced by a CE. Accordingly, the simulation results for the CE energetics are reliable only in the case of weak attenuation of the laser light intensity, as was shown by the
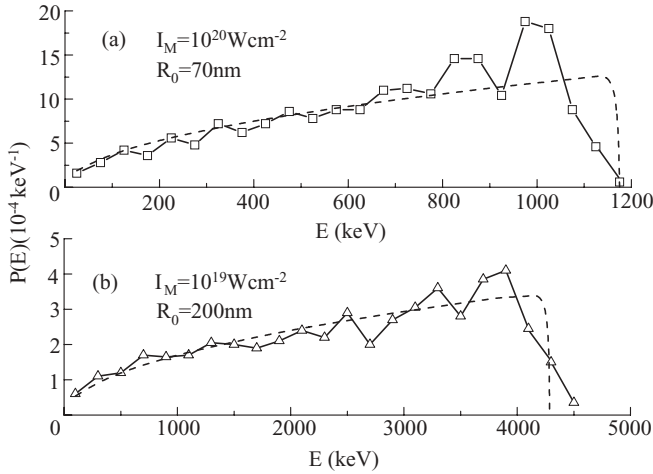
FIG. 5. Proton kinetic-energy distributions $P(E)$ in a CE of hydrogen nanodroplets for $R_0 = 70$ nm at $I_M = 10^{20}$ W cm^{-2} (upper panel) and for $R_0 = 200$ nm at $I_M = 10^{19}$ W cm^{-2} (lower panel). The SEID simulation results ($\square$ and $\triangle$) are connected by solid curves to guide the eye. The dashed curves (- – -) represent the theoretical results, Eq. (12), for complete and vertical outer ionization.

energy balance considerations [25]. The attenuation inside a single droplet is determined by the ratio

$$\zeta = E_{\text{fl}}/E_{\text{abs}} \qquad (13)$$

between the laser energy flow E_{fl} through the nanodroplet and the absorbed energy E_{abs}. We take [25] $E_{\text{fl}} = \pi \int dt\, I(t) R^2(t)$, where $R(t)$ is the radius of the expanding nanodroplet at time t and the integration is taken over the Gaussian laser pulse intensity $I(t)$. $E_{\text{abs}} = n E_{\text{av}}/\eta$, where n is the number of protons in the nanodroplet, η is the fraction of ion energy, and $1-\eta$ is the fraction of electron energy [38], with $\eta = 0.55$–0.87 [38–41]. In what follows we shall use the average value of $\eta = 0.7$. On the basis of previous work [25], we assert that the effects of light intensity attenuation are of minor importance and that the simulation results are reliable for $\zeta > 1$. Even for $\zeta \sim 1$, the damping of the proton energetics by light attenuation is still weak, so that the simulation results for the energetics are still reliable when ζ is slightly lower than unity. Using the expressions for E_{fl} [25] and for E_{abs} [38], we calculated the ζ parameters, which are presented in Fig. 6 for all the nanodroplets at $I_M = 10^{18}$ W cm^{-2} and at $I_M = 10^{19}$ W cm^{-2}, and for $R_0 = 140$ and 200 nm at $I_M = 10^{20}$ W cm^{-2}. At $I_M = 10^{20}$ W cm^{-2}, the parameter ζ is large, e.g., $\zeta = 9$ for $R_0 = 200$ nm and $\zeta = 75$ for $R_0 = 100$ nm, demonstrating the absence of any noticeable light attenuation. The situation is opposite at $I_M = 10^{18}$ W cm^{-2}, with the parameter ζ being smaller than unity for all nanodroplets except for $R_0 = 70$ nm (Fig. 6). At $I_M = 10^{19}$ W cm^{-2}, $\zeta > 1$ for all the nanodroplets studied by us except for the largest ($R_0 = 200$ nm) nanodroplet (Fig. 6), where $\zeta = 0.74$ is slightly smaller than 1. On the basis of this analysis, we shall consider the simulation results obtained for all the nanodroplets at $I_M = 10^{19}$ and 10^{20} W cm^{-2} to satisfy the condition of weak intra-nanodroplet laser intensity attenuation.
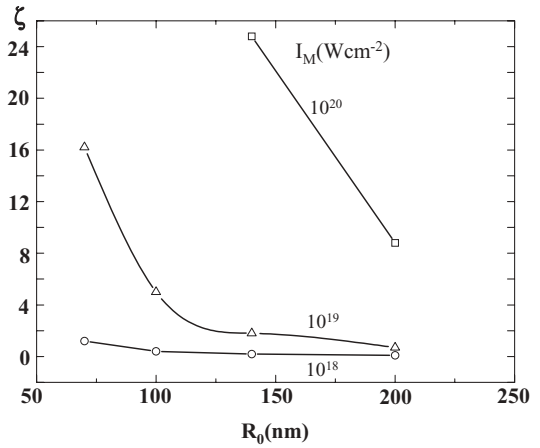

FIG. 6. The nanodroplet size and the laser intensity dependence of the ratio $\zeta = E_{\text{fl}}/E_{\text{abs}}$ [Eq. (13)] between the energy flow and the absorbed energy.

D. Averaged reaction probabilities

Using the energy distribution functions $P(E)$ that were obtained from SEID simulations, i.e., the data in Fig. 5, we calculated the averaged reaction probabilities $\langle y \rangle$, Eq. (3), for all cases that do not manifest significant effects of intra-nanostructure laser light attenuation (i.e., $\zeta > 1$ or $\zeta \sim 1$; see Sec. III C). These encompass all the nanodroplets treated by us at the intensities of $I_M = 10^{20}$ and 10^{19} W cm^{-2} (Fig. 6). The size dependence of $\langle y \rangle$ on the nanodroplet radius R_0 presented in Fig. 7 is stronger at $I_M = 10^{20}$ W cm^{-2} than at $I_M = 10^{19}$ W cm^{-2}, but in both cases this dependence is not steep. Thus the increase of radius R_0 by a factor of 2.9 (i.e., an increase in the number of atoms by a factor of 23) leads to a moderate increase of $\langle y \rangle$ by ~ 9 at $I_M = 10^{20}$ W cm^{-2} and ~ 5 at $I_M = 10^{19}$ W cm^{-2}.
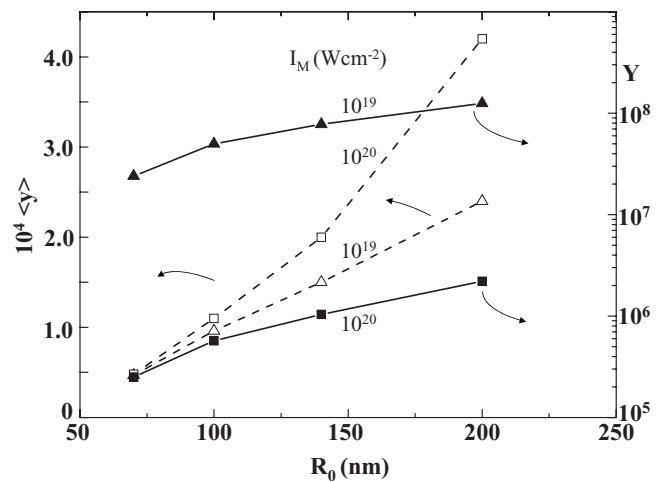

FIG. 7. The dependence of the averaged reaction probabilities $\langle y \rangle$ and the total ^{11}B$(p,\alpha)2\alpha$ fusion yields Y on the nanodroplet size and laser peak intensity. The calculations were performed in the size and laser parameter domains where weak laser intensity attenuation prevails both within a single nanodroplet and within the assembly of nanodroplets.

E. Number of protons within the plasma filament

To determine the fusion yields Y per pulse, Eq. (2), one requires estimates of the number of protons N_p in the plasma filament generated by a CE. The volume of the plasma filament, where those protons that are capable of contributing to the reaction yield are generated, will be described in a simplified way as a cylinder with the radius of the laser beam waist R_w and with the length $2L_{\mathrm{Ray}}$, where

$$L_{\mathrm{Ray}} = \pi R_w^2 / \lambda \qquad (14)$$

is the Rayleigh length. Figure 1 portrays a schematic description of the plasma filament. The radiation intensity $I(t)$ inside this plasma filament is assumed to be homogeneous and equal to the intensity at the laser beam waist. It is also assumed that the entire laser beam passes through the waist area πR_w^2. The time-integrated energy flow of the Gaussian pulse through the laser beam waist is taken to be equal to the laser pulse energy W. One then obtains the following expression for the waist area at a given peak intensity I_M and width τ of the laser pulse:

$$\pi R_w^2 = 1.33 W / I_M \tau, \qquad (15)$$

with R_w being given in cm, W in J, I_M in W cm^{-2}, and τ in s. Equations (14) and (15) provide the number of protons

$$N_p = 3.54 \frac{\rho}{\lambda} \left(\frac{W}{I_M \tau} \right)^2, \qquad (16)$$

where ρ is the proton density (in cm^{-3}) inside the plasma filament. The number of protons exhibits the laser intensity dependence $N_p \propto I_M^{-2}$. Here we take the pulse energy of Ref. [19], i.e., W = 0.6 J. The proton density inside the plasma filament $\rho = 3 \times 10^{18}$ cm^{-3} is estimated from the data of Ref. [19]. With these parameters, Eq. (16) gives the values of $N_p = 5.2 \times 10^{13}$, 5.2×10^{11}, and 5.2×10^9 for $I_M = 10^{18}, 10^{19}$, and 10^{20} W cm^{-2}, respectively.

F. Attenuation of the laser beam within an assembly of nanodroplets

The evaluation of the averaged reaction probability $\langle y \rangle$ (Sec. III D) and the number of protons N_p (Sec. III E) allows for estimates of the fusion yields according to Eq. (2). These will be obtained for a homogeneous laser intensity within the plasma filament, with weak laser intensity attenuation along the light-propagation axis $2L_{\mathrm{Ray}}$, Eq. (14). Weak laser intensity attenuation by the nanodroplets assembly will be realized when the energy E_{tot} absorbed within the plasma filament (which is calculated for a homogeneous laser intensity) is smaller than the pulse energy W [25,38]. We introduce the parameter β for the fraction of laser energy absorbed by the nanodroplets

$$\beta = E_{\mathrm{tot}} / W \qquad (17)$$

and require that $\beta < 1$. We take $E_{\mathrm{tot}} = E_{\mathrm{ion}}/\eta$, where $E_{\mathrm{ion}} = N_p E_{\mathrm{av}}$ is the energy of the protons produced by a CE and $\eta = 0.7$ is the fraction of the ions energy (see Sec. III C). From this analysis, we infer that
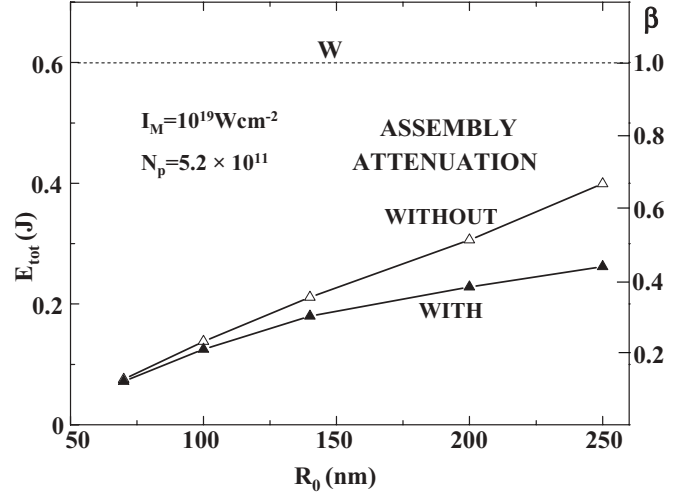
$$\beta = N_p E_{\mathrm{av}} / \eta W. \qquad (17')$$

FIG. 8. The effect of laser intensity attenuation by an assembly of nanodroplets. The size dependence of the energy E_{tot} absorbed within the plasma filament and the fraction β of the absorbed energy (for W = 0.6 J) were calculated using the parameters and procedure given in the text and are presented without attenuation ($\triangle$) and with attenuation ($\blacktriangle$).

The ratio β increases with the nanodroplet size R_0, as borne out by our calculations under the conditions of laser intensity homogeneity throughout the plasma filament. For the largest nanodroplet studied herein, $R_0 = 200$ nm at $I_M = 10^{20}$ W cm^{-2}, we calculate that $\beta = 0.01$, with the small value of β indicating a negligibly small assembly attenuation for all $R_0 \leqslant 200$ nm nanodroplets at this highest intensity. In Fig. 8, we present the β parameters calculated from Eq. (17') at $I_M = 10^{19}$ W cm^{-2} in the size domain $R_0 = 70-250$ nm, with the values of E_{av} being taken from Fig. 4. In the absence of attenuation, β increases almost linearly with increasing R_0, reaching relatively large values of $\beta = 0.51$ and 0.66 at $R_0 = 200$ and 250 nm, respectively, with β still being smaller than unity. These large values of β indicate the possibility of noticeable intensity assembly attenuation within the plasma filament. To estimate the assembly attenuation effect on the energy E_{tot} absorbed in the plasma filament [38], we solved the differential equation for the decrease of the laser intensity $I_M(x)$ along the laser propagation axis x [using Eq. (7) and nanoplasma parameters of Ref. [38] by linearly extrapolating the dependence of E_{av} on I_M. The calculated absorbed energies E_{tot} and the β parameters (Fig. 8) exhibit assembly attenuation effects. However, this attenuation of the absorbed energy by an assembly of nanodroplets with $R_0 \leqslant 200$ nm at $I_M = 10^{19}$ W cm^{-2} is not of considerable importance as β decreases only by 25% for $R_0 = 200$ nm at this intensity. For all other nanodroplet assemblies, $R_0 = 70$, 100, and 140 nm at $I_M = 10^{20}$ W cm^{-2}, and $R_0 = 70$ and 100 nm at $I_M = 10^{19}$ W cm^{-2}, we found that $\beta \simeq 0.1$–0.2, indicating the absence of any significant effects of intensity attenuation within the plasma filament. The calculations for the ^{11}B(p,α)2α fusion yields were performed in the size and laser intensity domains that satisfy the two conditions of weak laser intensity attenuation within the single nanodroplet (Sec. III C) and within the assembly of exploding

nanodroplets in the macroscopic plasma filament considered herein.

IV. REACTION PROBABILITIES AND YIELDS

The averaged reaction probabilities $\langle y \rangle$ and the total yields Y for the ^{11}B$(p,\alpha)2\alpha$ fusion reaction (Fig. 7) manifest the following features:

(i) The moderately high values of $\langle y \rangle \simeq 10^{-4}-10^{-5}$ (per proton) mark effective reactivity within the solid ^{11}B target.

(ii) The high values of the total yields, which reach $Y = 10^8$ (per laser pulse) for the solid ^{11}B cylindrical target, are considerably higher than the roughly estimated yields ($\sim 10^4-10^5$, see Sec. I) for this reaction within a plasma filament produced from CE of $(^{11}$B$_2H_6)_n$ hetero-nanodroplets.

(iii) The size dependence of the fusion yields manifests the increase of both the reaction probability $\langle y \rangle$ and the total yield Y with increasing R_0. These limited data (Fig. 7) indicate a power law of the form $\langle y \rangle \propto R_0^\alpha$, with $\alpha \simeq 1.6-2.3$, being essentially attributed to the increase of the proton energies with increasing the nanodroplet size.

(iv) The laser intensity dependence of the average reaction probability $\langle y \rangle$ at a fixed nanodroplet size reveals that it increases with increasing I_M (Fig. 7). The highest value of the averaged reaction probability $\langle y \rangle$ is attained at the highest intensity of $I_M = 10^{20}$ W cm^{-2} and for the largest nanodroplet size ($R_0 = 200$ nm). These laser and nanodroplet size parameters correspond to efficient outer ionization of the nanodroplet, resulting in the highest proton energies (Fig. 5).

(v) The yields Y for a fixed cluster size decrease with increasing I_M in the intensity range $I_M = 10^{19}-10^{20}$ W cm^{-2} (Fig. 7), with the highest values of the yield being attained at $I_M = 10^{19}$ W cm^{-2}. This effect manifests the strong dependence of N_p on I_M, i.e., $N_p \propto I_p^{-2}$, Eq. (16), due to the decrease of the reaction volume at higher intensities.

The dependence of Y on the nanodroplet size and on the laser intensity was determined for fixed values of the laser energy W and pulse length τ. Under these conditions, the maximal fusion yields were attained for nanodroplets with $R_0 = 200$ nm, which constitutes the largest nanodroplet size used herein, driven by a laser with $I_M = 10^{19}$ W cm^{-2} (Fig. 7). Regarding the value of R_0, we note that the upper size limit for $(H)_n$ nanodroplets is determined by the packing relation $n_{nd} = N_p/n > 1$. Here n_{nd} is the number of nanodroplets within the plasma filament and N_p is given by Eq. (16). This packing relation implies that for the laser parameters $I_M = 10^{20}$ W cm^{-2}, $\tau = 30$ fs, and W $= 0.6$ J used in our calculations, the nanodroplet upper size limit is $R_0 = 200$ nm, so that at our highest intensity the nanodroplet size cannot be further increased. The maximal fusion yield in the practical size domain of $R_0 = 200$ nm is attained for $I_M = 10^{19}$ W cm^{-2}. The fraction of absorbed laser energy by an assembly of such nanodroplets (Sec. III F) is $\beta = 0.4$ (Fig. 8), signifying efficient laser-nanodroplet energy transfer.

The efficiency parameter Φ for the fusion reaction will be defined by the ratio of the reaction yield Y, Eq. (2), and by the laser pulse energy, so that

$$\Phi = Y/W. \tag{18}$$

The source-target reaction design (Fig. 1) gives the maximal yield of $Y = 1.2 \times 10^8$ per pulse (Fig. 7) for W $= 0.6$ J, resulting in a high reaction efficiency of $\Phi = 2 \times 10^8$ J^{-1}.

V. DISCUSSION

The features of the reaction design, which produces high ($\sim 10^8$ per pulse) fusion yields between two distinct nuclei, are as follows: (i) It involves a source (i.e., an assembly of Coulomb exploding homonuclear hydrogen nanodroplets) of high-energy nuclei of one type (i.e., protons) and a target (i.e., a cylinder of solid ^{11}B) containing nuclei of the second type. (ii) The source and the target are spatially separated from each other. (iii) The target collects almost all the high-energy nuclei produced from the source. (iv) The solid target is sufficiently thick relative to the penetration depth, Eq. (7), to stop all the protons. (v) The source is driven by an ultra-intense, femtosecond laser pulse.

The yields and reaction efficiencies calculated herein using the source-target reaction design are considerably higher than those experimentally obtained and theoretically estimated by Belyaev *et al.* for the H + ^{11}B reaction driven by laser pulse irradiation of a boron polymer mixed ^{11}B + (CH$_2$)$_n$ solid [28,30]. These experiments used 1.5 ps pulses with a pulse energy of W $= 10$ J and provided a yield of $Y = 10^4$ per pulse, while the optimized theoretical estimates resulted in $Y = 10^5$ per pulse in the irradiated solid [30]. The reaction efficiency, Eq. (18), for the irradiated mixed solid is $\Phi = 10^3-10^4$ J^{-1}, which is lower by four to five orders of magnitude than that obtained in the present reaction design. The advantageous use of the nanodroplets source-cylindrical target design for the ^{11}B$(p,\alpha)2\alpha$ fusion based on a CE of hydrogen nanodroplets inside a ^{11}B cylinder leads to high table-top fusion yields ($\sim 10^8$ per pulse) relative to the yields from an irradiated mixed ^{11}B + (CH$_2$)$_n$ solid ($Y = 10^4-10^5$ per pulse [30]) and from the macroscopic plasma filament produced by a CE of $(B_2H_6)_n$ nanodroplets ($Y \sim 10^5$, as roughly estimated in Sec. I). It should be noted that the yields for ^{11}B$(p,\alpha)2\alpha$ fusion in all three of these systems are very large in comparison with other table-top fusion reactions [18,25,42]. These high yields are due to the large cross sections for this reaction (Sec. III A and Fig. 3), which are responsible for the five orders of magnitude increase of the yield for ^{11}B$(p,\alpha)2\alpha$ fusion in CE of $(B_2H_6)_n$ nanodroplets relative to the $^{12}C(p,\gamma)^{13}$N fusion in a CE of (CH$_4$)$_n$ nanodroplets [25] (as discussed in Sec. I). What is even more interesting is the marked enhancement by three to four orders of magnitude of the ^{11}B$(p,\alpha)2\alpha$ table-top fusion yield within the source-target reaction design used herein (Fig. 1) on the one hand, and those yields in laser-irradiated mixed ^{11}B + (CH$_2$)$_n$ solids [30] and in the macroscopic plasma filament produced by CE of $(B_2H_6)_n$ nanodroplets (Sec. I) on the other hand. The high yield for the homonuclear nanodroplet source-cylindrical target can be rationalized in terms of the cumulative contribution of several effects originating from the properties of the target and of the source, all of which lead to the increase of the yield. The properties of the cylindrical target involve the efficient collection of all high-energy protons from the source (Fig. 1), together with a moderately low stopping power and large penetration depths of protons within solid ^{11}B (Secs. II C, III A,

and Fig. 2). Regarding the properties of the source, these involve low assembly attenuation effects for laser energy acquisition by the protons produced by a CE of homonuclear hydrogen nanodroplets (Sec. III F), leading to high-energy protons from exploding large nanodroplets. On the other hand, a CE in an irradiated mixed boron-carbon-hydrogen solid or in an assembly of heteronuclear boron-hydrogen nanodroplets under the conditions of large energy acquisition by the nanodroplets assembly will result in sharing of the energy between the protons and the heavy nuclei, leading to the reduction of the proton kinetic energy and consequently of the fusion yield. In the case of optimized fusion conditions, when a significant fraction of the laser energy is absorbed by the assembly of the irradiated nanodroplets, it is preferable to use homonuclear systems as the source of the energetic light nuclei. The cumulative contributions from all these effects will result in efficient high-yield, table-top aneutronic fusion.

A key element of the efficient table-top fusion scheme explored herein rests on the attainment of high (MeV) proton kinetic energies in a CE of nanodroplets. Our SEID molecular-dynamics simulations [37] account for all the interparticle Coulomb interactions and for all the charged particle–laser interactions. A basic approximation involved in the simulations (apart from the application of an adequate classical simulation scheme) involves the neglect of proton-electron collisions, which is justified [23,34]. The collective effects advanced for the description of outer ionization of large finite systems, i.e., plasma resonances [33,43], hydrodynamic pressure originating from hot electron plasmas [43], and superintense radiation pressure effects [43], are incorporated in the results of the computational scheme. It is interesting to identify the fingerprints of these collective effects in the simulation results and to elucidate unique features of outer ionization and CE of nanostructures in superintense ($I_M = 10^{19}-10^{20}$ W cm^{-2}) laser fields. In analogy to clusters [34], it appears that the major

mechanism for outer ionization of nanodroplets involves field ionization [25,26]. The possible effects of plasma resonances in clusters were described [33,43] in terms of a homogeneous distribution of the persistent nanoplasma electrons within the Coulomb exploding nanostructure. Theoretical studies of the effect of nanoplasma electrons on CE of deuterium [34] and elemental [44] clusters provided evidence for a lychee model [34,44], where the persistent nanoplasma forms an inner neutral sphere while the ions form an electron-free exterior shell. The exploration and implications of the lychee model to nanodroplets will be of interest. In the context of radiation pressure effects [43], outer ionization and CE of nanodroplets driven by superintense lasers ($I_M = 10^{19}-10^{20}$ W cm^{-2}) will be markedly affected by the magnetic radiation field. Magnetic-field-induced radiation pressure will be manifested in spatial anisotropy of protons in the CE of nanodroplets. These features of radiation-nanostructure interactions deserve further exploration.

The use of the exploding nanodroplet source-cylindrical solid target considered herein is not limited to the ^{11}B$(p,\alpha)2\alpha$ aneutronic fusion and will be applicable for the exploration of other high-yield table-top fusion reactions. An interesting application of this table-top experimental design will involve the $^7Li(p,n)^7$Be fusion reaction [45], which is of interest in the context of conversion of high-energy protons into high-energy neutrons [46]. Another interesting application of aneutronic ^{11}B$(p,\alpha)2\alpha$ fusion will involve the generation of ultrashort pulses of α particles on the picosecond time scale, providing additional features of time-resolved pulses of particles, i.e., neutrons [42,47], γ [25], and α in table-top fusion experiments.

[1] J. M. Dawson, in *Fusion*, edited by E. Teller (Academic, New York, 1981),Vol. 1, Pt. B, p. 453.

[2] S. Eliezer, Z. Henis, and J. M. Martinez-Val, Nucl. Fusion **37**, 985 (1997).

[3] W. M. Nevins and R. Swain, Nucl. Fusion **40**, 865 (2000).

[4] S. Son and N. J. Fisch, Phys. Lett. A **329**, 76 (2004).

[5] D. C. Moreau, Nucl. Fusion **17**, 13 (1977).

[6] H. R. Yousefi, T. Haruki, J. I. Sakai, A. Lumanta, and K. Masugata, Phys. Lett. A **373**, 2360 (2009).

[7] N. Rostoker, M. W. Binderbauer, and H. J. Monkhorst, Science **278**, 1419 (1997).

[8] A. F. Lifschitz, R. Farengo, and N. R. Arista, Phys. Plasmas **7**, 3036 (2000).

[9] J. M. Martinez-Val, S. Eliezer, M. Piera, and G. Velarde, Phys. Lett. A **216**, 142 (1996).

[10] H. Hora, G. H. Miley, M. Ghoranneviss, B. Malekynia, N. Azizi, and X-T. He, Energy Environ. Sci. **3**, 479 (2010).

[11] N. Azizi, H. Hora, G. H. Miley, B. Malekynia, M. Ghoranneviss, and X. He, Laser Part. Beams **27**, 201 (2009).

[12] W. M. Nevins and A. Carlson, Science **281**, 307a (1998).

[13] H. Hora, G. H. Miley, M. Ghoranneviss, B. Malekynia, and N. Azizi, Opt. Commun. **282**, 4124 (2007).

[14] J. Zweiback, R. A. Smith, T. E. Cowan, G. Hays, K. B. Wharton, V. P. Yanovsky, and T. Ditmire, Phys. Rev. Lett. **84**, 2634 (2000).

[15] V. P. Krainov and M. B. Smirnov, Phys. Rep. **370**, 237 (2002).

[16] A. Heidenreich, J. Jortner, and I. Last, Proc. Natl. Acad. Sci. USA **103**, 10589 (2006).

[17] G. R. Mourou, T. Tajima, and S. V. Bulanov, Rev. Mod. Phys. **78**, 309 (2006).

[18] V. P. Krainov, B. M. Smirnov, and M. B. Smirnov, Phys. Usp. **50**, 907 (2007).

[19] S. Ter-Avetisyan, M. Schnürer, D. Hilscher, U. Jahnke, S. Busch, P.V. Nicles, and W. Sandner, Phys. Plasmas **12**, 012702 (2005).

[20] D. Umstadter, J. Phys. D **36**, R151 (2003).

[21] K. W. Madison, P. K. Patel, D. Price, A. Edens, M. Allen, T. E. Cowan, J. Zweiback, and T. Ditmire, Phys. Plasmas **11**, 270 (2004).

[22] H. Y. Lu *et al.*, Phys. Rev. A **80**, 051201(R) (2009).

[23] I. Last and J. Jortner, Phys. Rev. A **64**, 063201 (2001).

[24] I. Last and J. Jortner, Phys. Rev. Lett. **97**, 173401 (2006).

[25] I. Last and J. Jortner, Phys. Plasmas **14**, 123102 (2007).

[26] I. Last and J. Jortner, Phys. Rev. A **77**, 033201 (2008).

[27] H. Schwoerer, P. Gibbon, S. Düsterer, R. Behrens, C. Ziener, C. Reich, and R. Sauerbrey, Phys. Rev. Lett. **86**, 2317 (2001).

[28] V. S. Belyaev, A. P. Matafonov, V. I. Vinogradov, V. P. Krainov, V. S. Lisitsa, A. S. Roussetski, G. N. Ignatyev, and V. P. Adrianov, Phys. Rev. E **72**, 026406 (2005).

[29] A. Yossef, R. Kodama, and M. Tampo, Phys. Plasmas **13**, 030701 (2006).

[30] V. S. Belyaev *et al.*, Phys. At. Nucl. **72**, 1077 (2009).

[31] V. P. Krainov, Laser Phys. Lett. **2**, 89 (2005).

[32] J. Davis, G. M. Petrov, and A. L. Velikovich, Phys. Plasmas **13**, 064501 (2006).

[33] U. Saalmann, Ch. Siedschlag, and J. M. Rost, J. Phys. B **39**, R39 (2006).

[34] I. Last and J. Jortner, Phys. Rev. A **73**, 013202 (2006).

[35] H. H. Andersen and J. F. Ziegler, *Hydrogen Stopping Powers and Ranges in All Elements*, (Pergamon, New York, 1977).

[36] D. J. Rose and M. Clark Jr., *Plasmas and Controlled Fusion*, (MIT Press, Cambridge, MA, 1961).

[37] I. Last and J. Jortner, Phys. Rev. A **75**, 042507 (2007).

[38] I. Last and J. Jortner, Phys. Rev. A **73**, 063201 (2006).

[39] P. B. Parks, T. E. Cowan, R. B. Stephens, and E. M. Campbell, Phys. Rev. A **63**, 063203 (2001).

[40] M. Eloy, R. Azambrya, T. M. Mendonca, and R. Brigham, Phys. Plasmas **8**, 1084 (2001).

[41] V. S. Belyaev, V. P. Krainov, V. S. Lisitsa, and A. P. Matafonov, Phys. Usp. **51**, 793 (2008).

[42] K. W. Madison, P. K. Patel, M. Allen, D. Price, R. Fitzpatrick, and T. Ditmire, Phys. Rev. A **70**, 053201 (2004).

[43] Th. Fennel, K.-H. Meiwes-Broer, J. Tiggesbäumker, P.-G. Reinhard, P. M. Dinh, and E. Suraud, Rev. Mod. Phys. **82**, 1793 (2010).

[44] A. Heidenreich, I. Last, and J. Jortner, Phys. Chem. Chem. Phys. **11**, 111 (2009).

[45] D. P. Higgenson *et al.*, Phys. Plasmas **17**, 100701 (2010).

[46] K. L. Lancaster *et al.*, Phys. Plasmas **11**, 3404 (2004).

[47] J. Zweiback, T. E. Cowan, R. A. Smith, J. H. Hartley, R. Howell, C. A. Steinke, G. Hays, K. B. Wharton, J. K. Crane, and T. Ditmire, Phys. Rev. Lett. **85**, 3640 (2000).